JACS
JOURNAL OF THE AMERICAN CHEMICAL SOCIETY
pubs.acs.org/JACS
Article

Reversible Electrochemical Anionic Redox in Rechargeable Multivalent-Ion Batteries

Ankur L. Jadhav, Taylor R. Juran, Matthew A. Kim, Andrea M. Bruck, Brendan E. Hawkins, Joshua W. Gallaway,* Manuel Smeu,* and Robert J. Messinger*

Cite This: J. Am. Chem. Soc. 2023, 145, 15816−15826

ABSTRACT: Rechargeable multivalent-ion batteries are of significant interest due to the high specific capacities and earth abundance of their metal anodes, though few cathode materials permit multivalent ions to electrochemically intercalate within them. The crystalline chevrel phases are among the few cathode materials known to reversibly intercalate multivalent cations. However, to date, no multivalent-ion intercalation electrodes can match their reversibility and stability, in part due to the lack of design rules that guide how ion intercalation and electron charge transfer are coupled up from the atomic scale. Here, we elucidate the electronic charge storage mechanism that occurs in chevrel phase (Mo_6Se_8, Mo_6S_8) electrodes upon the electrochemical intercalation of multivalent cations (Al^{3+}, Zn^{2+}), using solid-state nuclear magnetic resonance spectroscopy, synchrotron X-ray absorption near edge structure measurements, operando synchrotron diffraction, and density functional theory calculations. Upon cation intercalation, electrons are transferred selectively to the anionic chalcogen framework, while the transition metal octahedra are redox inactive. This reversible electrochemical anionic redox, which occurs without breaking or forming chemical bonds, is a fundamentally different charge storage mechanism than that occurring in most transition metal-containing intercalation electrodes using anionic redox to enhance energy density. The results suggest material design principles aimed at realizing new intercalation electrodes that enable the facile electrochemical intercalation of multivalent cations.

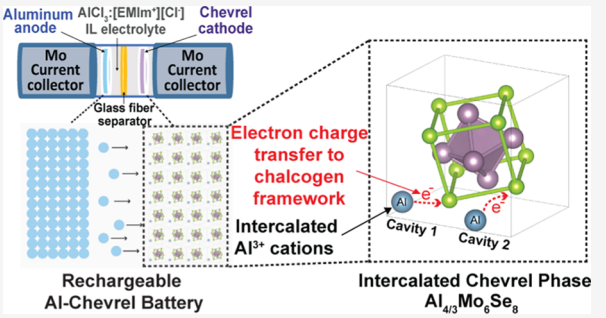

INTRODUCTION

Lithium-ion batteries revolutionized portable electronics, but critical improvements are required in energy density, cycle life, safety, and cost to electrify transportation and integrate renewable energy sources into the electric grid on a global scale.[1−3] Batteries that use multivalent cations (e.g., Mg^{2+}, Ca^{2+}, Zn^{2+}, and Al^{3+}) as the electroactive species transfer multiple electrons per ion, resulting in high specific capacities.[3,4] Their corresponding metal anodes (Mg, Ca, Zn, and Al) are earth-abundant, low-cost, energy-dense metals, some of which are intrinsically safe (Zn, Al).[5] Unlike lithium cations, the electrodeposition of multivalent cations is often relatively uniform, mitigating dendrite formation.[2,6] Due to their smaller size compared to monovalent ions, multivalent-ion intercalation into crystalline compounds results in minimal volume expansion, a key factor in long-cycle life batteries.[7] However, reversible multivalent-ion intercalation into crystalline electrode materials is challenging due to high ionic charge densities, resulting in slow solid-state ionic diffusion within the host crystal structure.[8−12] Furthermore, desolvation of these highly charged ions adds higher energetic penalties at the electrode−electrolyte interface, requiring unique ion−solvent coordination structures that have thus far limited the number of compatible electrolytes for multivalent-ion battery systems.[3,5] Widespread use of multivalent battery chemistry has remained elusive, in part due to limited understanding and control of the complex electronic, chemical, and structural changes that the electrodes and their interfaces undergo upon ion intercalation.

The chevrel phases Mo_6X_8 (X = S, Se, or Te) are among the few materials known to electrochemically intercalate divalent (e.g., Mg^{2+}, Zn^{2+}, etc.)[6,12] and trivalent (Al^{3+}) cations.[8,13−15] Discovered by Chevrel in 1971[16] and introduced by Aurbach et al.[6] in 2000 as a positive electrode material for magnesium batteries, chevrel Mo_6S_8 has since acted as the quintessential Mg-ion intercalation electrode. The remarkable chevrel unit cell is composed of a Mo_6 octahedron caged within an X_8 chalcogen cube, which crystallizes into a structure with large cavities and an electronically polarizable framework that

Received: March 9, 2023
Published: July 13, 2023

https://doi.org/10.1021/jacs.3c02542
J. Am. Chem. Soc. 2023, 145, 15816−15826

enables fast ion diffusion.[17,18] Other unique chalcogen clusters have been reported that can electrochemically intercalate cations; for example, organometallic rhenium(III) chalcogenide clusters [Re_6Q_8 (Q = S, Se)] have also been synthesized and have successfully shown lithium cation insertion.[19,20]

While numerous studies have investigated ion intercalation mechanisms into chevrel-phase electrodes and their structural ramifications over the last two decades, particularly for Mg^{2+} cations, the electron charge transfer process is not well understood. The few studies investigating the electron charge transfer mechanism in Mg−Mo_6S_8 batteries have reported conflicting results. Using X-ray photoelectron spectroscopy, Richard et al.[21] reported that the additional electronic charge upon Mg^{2+} cation intercalation is distributed over both the Mo_6 clusters and S_8 (i.e., chalcogen) cubes in a two-step charge transfer process. On the contrary, Thole et al.[22] and Wan et al.[23] studied the charge transfer process theoretically and using ex situ X-ray absorption near edge structure (XANES) measurements, indicating that only the sulfur framework takes part in the electron charge transfer upon Mg^{2+} insertion.[19,20] A decisive understanding of the electron charge transfer and storage mechanism is a missing link, one that could help researchers better understand why the chevrel phase remains the dominant intercalation electrode for multivalent ions batteries while leading to material design principles aimed at new multivalent intercalation electrodes with improved electrochemical properties. Furthermore, regarding the ion charge storage mechanism, it has been shown that multivalent ions intercalate into chevrel Mo_6S_8 differently depending on their charge density, as shown for Mg^{2+} ions[15,24,25] and Al^{3+} ions,[15,24,25] though the consequences on the electron charge storage mechanism remain unclear.

In parallel, researchers have been striving to increase the energy density of Li-ion battery cathodes by leveraging anionic redox, particularly in lithium-rich transition metal oxides and chalcogenides. In most traditional Li-ion batteries using transition metal oxides (e.g., NMC) as electrode materials, the electrons are stored and distributed over the d-orbitals of the transition metals, which are redox active.[26] However, oxygen anionic redox has been the subject of intense investigation, which has been observed at higher potentials in Li or Na-rich transition metal oxides such as Li-rich NMC ($Li_{1+x}Ni_yCo_zMn_{(1-x-y-z)}O_2$) and Ru-containing layered oxide compounds ($Li_2Ru_{1-y}Sn_yO_3$).[27−30] This electrochemical anionic redox enhances the energy density due to additional specific capacity at higher voltage; however, oxygen anionic redox typically leads to structural instabilities and side reactions that result in capacity fade. Interestingly, anionic redox has been demonstrated in lithium-rich chalcogenides, including lithium-rich titanium sulfides ($LiTiS_2$−Li_2TiS_3 family),[31] lithium-rich iron sulfides Li_2FeS_2 and $LiNaFeS_2$,[32] and the solid solution $Li_2FeS_{2-y}Se_y$.[33] These electrode systems function by coupling the cationic redox of the transition metals with the anionic redox of the chalcogen atoms. Notably, all of the above materials contain an excess of lithium, where transition metal redox activity alone is not sufficient to charge balance the excess Li inserted. Thus, researchers have been searching for unique electron storage mechanisms, including anionic redox processes, that can be used in rechargeable battery electrodes to enhance energy density without affecting electrode stability and electrochemical reversibility.

Here, we elucidate that chevrel-phase electrodes undergo reversible electrochemical anionic redox upon the intercalation of multivalent cations, which occurs without breaking or forming chemical bonds. While the chalcogen framework is redox active, the transition metal octahedra are redox inactive. We study trivalent Al^{3+} cation intercalation into chevrel Mo_6Se_8 for the first time using electrochemical, spectroscopic, diffraction, and computational methods, comparing its electrochemical, structural, and electronic properties to chevrel Mo_6S_8. The anionic electron charge transfer mechanism is shown to be general, occurring also for divalent Zn^{2+} cation intercalation into chevrel Mo_6Se_8. The results suggest that anionic redox may be incorporated as a molecular-level material design principles aimed at realizing new multivalent-ion battery intercalation electrodes with enhanced ion intercalation and diffusion properties.

METHODS

Chevrel Phase Synthesis. $Cu_2Mo_6S_8$ and $Cu_2Mo_6Se_8$ were synthesized via a solid-state synthesis in a procedure similar to the one used by Saha et al.[34] In a typical synthesis, 1.2 g of molybdenum powder (Mo, Alfa Aesar, 99.9%), 0.8 g of copper sulfide or 1.18 g of copper selenide (CuS/CuSe, Alfa Aesar, 99.9%), and 2.0 g of molybdenum disulfide or 3.17 g of molybdenum diselenide (MoS_2/$MoSe_2$, Alfa Aesar, 99.9%) were ball-milled for 3 h. The solid mixture was then placed in a tube furnace at 1000 °C for 7 h under an ultra-high purity argon atmosphere to form crystalline $Cu_2Mo_6X_8$ (X = Se, Se). The solid powder of $Cu_2Mo_6X_8$ was then mixed with a 6 M HCl solution for 8 h at room temperature under constant air bubbling, which leaches the copper into solution, forming crystalline Mo_6S_8 or Mo_6Se_8. The resulting precipitate was filtered from the solution, rinsed twice with ethanol and once with water, and then dried under vacuum at 90 °C overnight.

Composite Electrode Preparation. To prepare the chevrel-phase composite electrode, chevrel (80 wt. % of the composite electrode) and carbon black (10 wt. %) (Super P, Alfa Aesar, 99%) were ball-milled in the glovebox for 1 h. In a glass vial, polyvinylidene fluoride (PVDF, Sigma-Aldrich, average molecular weight 534,000 g/mol) binder (10 wt. %) was dissolved in *N*-methyl-2-pyrrolidone (NMP), and the ball-milled chevrel-carbon mixture was added to the solution. The mixture was ultra-sonicated for 30 s and mixed well to form an electrode slurry, which was then cast on Mo foil (Alfa Aesar, 99.95%, 0.025-mm thick, used for Al-chevrel cells) or stainless-steel foil (McMaster-Carr, 0.1-mm thick, used for Zn-chevrel cells) using an MTI film coater and doctor blade. The casted sheet was dried in a vacuum oven at 120 °C overnight to evaporate the NMP solvent. The final electrode thickness was ca. 120 μm.

Electrochemical Cell Assembly. Rechargeable Al-chevrel cells were constructed in an argon-filled glovebox (<1 ppm O_2 and H_2O). Polytetrafluorethylene (PTFE) Swagelok unions with a diameter of either 1/4-in or 1/2-in were used to assemble airtight cells. Molybdenum rods were used as current collectors for both electrodes. Aluminum foil (MTI, 99.99%, 0.1-mm thick) was used as an anode. Circular electrodes of 6-mm or 11-mm diameter were used in 1/4-in or 1/2-in Swagelok cells, respectively. A glass microfiber filter (GF/D, Whatman) was used as a separator. Aluminum chloride:1-ethyl-3-methylimidazolium chloride (Iolitec, $AlCl_3$:[EMIm]Cl, molar ratio 1.5:1) ionic liquid was used as an electrolyte (40 μL or 120 μL for 1/4-in or 1/2-in Swagelok cells, respectively). The electrodes, separator, and electrolyte were compressed by the current collector rods on both sides. Rechargeable Zn-chevrel cells were assembled using a similar process, except: (i) zinc foil (Alfa-Aesar, 99.98%, 0.25-mm thick) was used as the anode, (ii) 1 M aqueous $Zn(SO_4)_2$ solution was used as the electrolyte, (iii) the composite chevrel electrodes were cast on stainless steel, while stainless steel current collector rods were used with PTFE Swagelok unions.

Electrochemical Measurements. Galvanostatic cycling and cyclic voltammetry (CV) were performed on an Arbin LBT battery tester and Metrohm Autolab potentiostat (PGSTAT302N), respectively. The higher temperature (50 °C) electrochemical measure-

https://doi.org/10.1021/jacs.3c02542
J. Am. Chem. Soc. 2023, 145, 15816−15826

ments were performed in a Thermo Scientific Heratherm Oven. For Al−Mo_6Se_8 and Zn−Mo_6Se_8 batteries, the upper cut-off potentials were 1.20 and 0.80 V, respectively, while the lower cut-off potentials were 0.05 and 0.30 V. For CV experiments, a scan rate of 20 μV/s or 50 μV/s was used for Al-chevrel or Zn-chevrel cells, respectively.

Sample Preparation for NMR Spectroscopy. All Al-chevrel cells were disassembled inside an argon-filled glovebox (<1 ppm O_2 and H_2O). The Al-chevrel electrodes were rinsed three times in anhydrous methanol and dried in the glovebox. The samples were then stripped from the current collector foil, crushed using a mortar and pestle, and packed into a 1.6-mm diameter zirconia rotor inside the glovebox. All Zn-chevrel cells were disassembled under ambient conditions. The Zn chevrel electrodes were rinsed three times with deionized water, dried under vacuum at 60 °C, and then packed within the 1.6-mm zirconia rotors.

Solid-State NMR Spectroscopy. Solid-state ^{77}Se, ^{95}Mo, and ^{27}Al nuclear magnetic resonance (NMR) spectra were acquired on a Bruker AVANCE III HD 600 MHz NMR spectrometer with a 14.1 T narrow-bore superconducting magnet operating at 114.45, 39.11, and 156.39 MHz, respectively. A PhoenixNMR 1.6-mm HXY magic-angle-spinning (MAS) probehead was used, where samples were rotated at MAS rates of 20 kHz. For ^{95}Mo measurements, a separate low-gamma accessory was used to tune to the ^{95}Mo frequency. Air at a temperature of 293.2 K was pumped through the probehead at 600 L/h to mitigate sample heating due to MAS. ^{77}Se, ^{95}Mo, and ^{27}Al shifts were referenced to selenous acid (H_2SeO_3, Alfa Aesar, 97%) at 1290 ppm, 2 M aqueous Na_2MoO_4 (Sigma-Aldrich, 99%) at 0 ppm, and 1 M aqueous $Al(NO_3)_3$ (Sigma-Aldrich, 99.997%) at 0 ppm, respectively.

For solid-state ^{77}Se and ^{95}Mo NMR spectra, spin-echo experiments were acquired to minimize acoustic ring-down effects. Solid-state ^{77}Se spin-echo experiments were acquired using an initial short rf pulse of 1.2 μs with a 52.1 kHz rf field strength to excite the broad ^{77}Se spectral range of Mo_6Se_8. Solid-state ^{95}Mo spin-echo NMR experiments were conducted with a $\pi/2$ pulse of 5 μs, calibrated with respect to 2 M aqueous Na_2MoO_4 ($\pi/2$ pulse of 5 μs, 50 kHz rf field strength). Solid-state ^{27}Al single-pulse experiments were conducted using a short $\pi/12$ pulse of 0.31 μs, calibrated with respect to 1 M aqueous $Al(NO_3)_3$ ($\pi/2$ pulse of 1.9 μs, 125 kHz rf field strength). Recycle delays of 0.05, 0.01, and 0.01 s were used for ^{77}Se, ^{95}Mo, and ^{27}Al NMR experiments, during which all spins relaxed to thermal equilibrium ($d_1 > 5*T_1$). Spectra were deconvoluted using the DMFit program.[35]

DFT Calculations. Density functional theory (DFT) calculations were carried out with the Vienna Ab initio Simulation Package (VASP),[36−38] utilizing the projector-augmented-wave (PAW) method[39] and the SCAN functional.[40] The energy sufficiently converged to <1 meV/atom for the $AlMo_6X_8$ unit cell, where X = S, Se, when setting the kinetic energy cutoff to 650 eV and the Γ-centered k-mesh to 5 × 5 × 5. For computational efficiency, this criterion was reduced for the 2 × 2 × 2 supercells; an energy cutoff of 450 eV and Γ-centered k-mesh of 1 × 1 × 1 was determined to be adequate. Spin polarization was not included in our calculations, as it was determined to not be necessary in our previous DFT study of chevrel Mo_6S_8 electrodes.[14]

Full structural and ionic relaxations were performed for bulk Al metal and $Al_MMo_6X_8$, where X = S, Se and M = 0 to 4/3. All chevrel phase structures are based on the $MgMo_6Se_8$ as studied by Levi et al.,[17,41] changing only the type of chalcogen or intercalant, not the position. For a battery consisting of a pure Al metal anode and a chevrel-phase cathode, the full cell electrochemical reaction is described by

$$Al_M + Mo_6X_8 \rightarrow Al_MMo_6X_8 \quad (1)$$

From the electronic structure calculations, the voltage can be calculated as the difference in total energies between the products and the reactants, normalized by the number of electrons transferred, according to

$$V = -\left(\frac{E(AlMo_6X_8) - E(Mo_6X_8) - E(Al)}{N_{electrons}}\right) \quad (2)$$

where $E(AlMo_6X_8)$ is the energy of the intercalated chevrel-phase cathode, $E(Mo_6X_8)$ is the energy of the empty chevrel-phase cathode, $E(Al)$ is the energy per atom of the Al metal anode, and $N_{electrons}$ is the number of electrons transferred with the cation.[42] Note that the voltage calculated by eq 2 is an approximation. The exact voltage calculation is dependent upon the Gibbs free energy rather than the change in internal energy. However, including changes in volume and entropy would result in a less than 0.1 V correction from the approach used here; therefore, the impact of doing so is negligible.[43]

Voltage profiles were calculated by expanding the unit cell to a 2 × 2 × 2 supercell. We performed a full ionic and structural relaxation for each of the possible $Al_MMo_6X_8$ configurations; the lowest energy structure was taken as the preferred configuration. Voltages were calculated according to eq 2, though here we compare the energy of the structure to the energy of the relaxed structure with one less intercalated Al ion [e.g., with n ions vs $(n - 1)$ Al ions].

EDXRD. Operando synchrotron energy dispersive X-ray diffraction (EDXRD) measurements were performed at beamline 6-BM-A at the Advanced Photon Source (APS) at Argonne National Laboratory. Diffraction data were collected on hermetically sealed gold-plated stainless-steel CR2032 coin cells without transparent windows or other modifications. This setup was possible because the incident white beam had an energy range from approximately 20−200 keV, sufficient to penetrate the cell. For this reason, there was no opportunity for oxidation or contamination of the chevrel electrode during extraction from the cell. Crystallographic data for Al-ion and Zn-ion batteries with both Mo_6S_8 and Mo_6Se_8 electrodes were collected as the cells were discharged on a low-profile hotplate at 60 °C. A MACCOR battery cycler was used to cycle the batteries at C/10.7 (12 mA/g) during EDXRD measurements at a constant angle of $2\theta = 3°$. The diffracted beam intensity was measured using a high-resolution germanium detector, while calibration from the detector channel to photon energy was performed using an α-Al_2O_3 standard. The diffraction gauge volume was 40 μm tall. The chevrel electrodes were profiled spatially; however, no inhomogeneity in the electrochemical intercalation reaction was observed in any cell. Thus, the data were taken from the centers of the electrode, which was representative of the cell. The data collection time per diffraction pattern was 60 s. EDXRD data are reported as a function of photon energy in keV, which can be converted to d-spacing by Bragg's law

$$d = \frac{hc}{2E \sin \theta_{EDXRD}} \quad (3)$$

where E is photon energy, θ_{EDXRD} is the diffraction angle, h is Planck's constant, and c is the speed of light.

XANES. Synchrotron XANES measurements were performed at NSLS-II beamline 7-BM (QAS). All measurements were performed in fluorescence mode, scanning the Mo K-edge.

RESULTS AND DISCUSSION

Electrochemical Al^{3+} Ion Intercalation into Chevrel Phase Electrodes. To experimentally measure the electron charge transfer to chevrel phase frameworks, we first electrochemically intercalated trivalent Al^{3+} cations into chevrel Mo_6Se_8. The selenium chalcogen frameworks enable solid-state ^{77}Se NMR measurements, which are highly sensitive to the local electronic environments of the Se_8 cubes. Note that solid-state ^{33}S NMR is challenging due to the very low natural abundance (0.76%), low gyromagnetic ratio (Larmor frequency of 46.08 MHz at 14.1 T), and quadrupolar nature (spin = 3/2) of ^{33}S nuclear spins. Solid-state ^{77}Se is more sensitive due to its higher natural abundance (7.63%), higher gyromagnetic ratio (Larmor frequency of 114.48 MHz at 14.1 T), and non-quadrupolar nature (spin = 1/2).

https://doi.org/10.1021/jacs.3c02542
J. Am. Chem. Soc. 2023, 145, 15816−15826

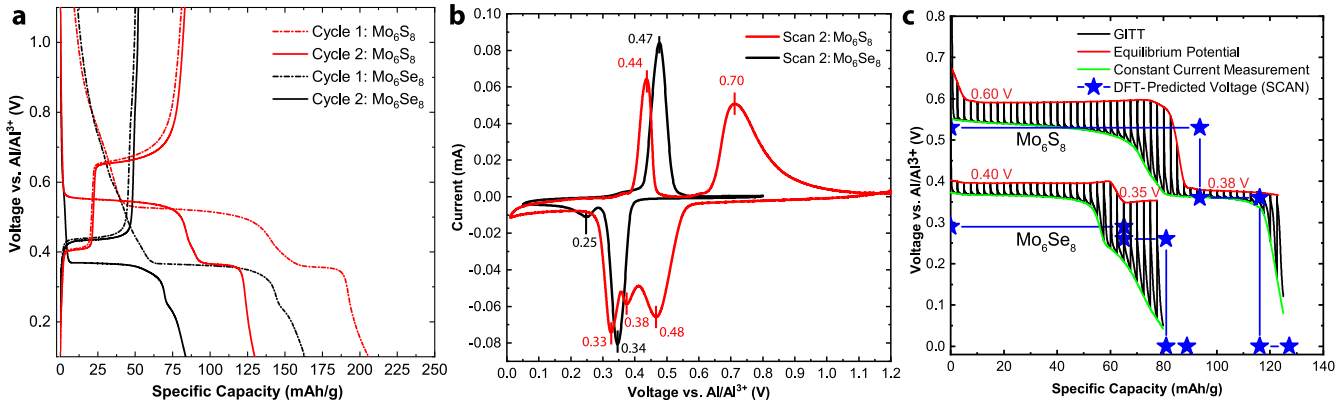

Figure 1. Electrochemical intercalation of Al^{3+} cations into chevrel phases with different anionic chalcogen frameworks. (a) Galvanostatic cycling (10 mA/g) of chevrel Mo_6S_8 (red) and chevrel Mo_6Se_8 (black) electrodes. Theoretical capacities were achieved upon second discharge (128 mA h/g for Mo_6S_8 and 88 mA h/g for Mo_6Se_8). (b) CV (20 μV/s, scan 2) on Al−Mo_6S_8 (red) and Al−Mo_6Se_8 (black) cells. (c) GITT measurements of Al−Mo_6S_8 and Al−Mo_6Se_8 cells with DFT-predicted potentials (SCAN functional). All electrochemical measurements were performed at 50 °C.

We thus prepared rechargeable Al−Mo_6Se_8 cells for the first time, analyzed their electrochemical properties, and compared them to Al−Mo_6S_8 cells (Figures 1 and S1). Galvanostatic cycling shows two distinct discharge plateaus where theoretical capacities of 88 and 128 mA h/g were achieved upon the second discharge for Mo_6Se_8 and Mo_6S_8 electrodes, respectively, corresponding to four electron transfers per Mo_6X_8 unit (Figure 1a). Additional capacities observed during the first cycles are associated with decomposition of the ionic liquid electrolyte and the formation of a surface layer upon desolvation of Al^{3+} from the chloroaluminate anions.[8,13,15] Al^{3+} cations electrochemically intercalate into Mo_6Se_8 at lower potentials compared to Mo_6S_8, consistent with our DFT calculations described below, as well as Levi and Aurbach's work on Mg^{2+} cation intercalation into Mo_6Se_8 and Mo_6S_8 electrodes.[18,44] CV reveals two distinct reduction peaks (0.34 and 0.25 V) for Mo_6Se_8 as opposed to three peaks for Mo_6S_8 (0.48, 0.38, and 0.33 V) (Figure 1b), all of which are due to Al^{3+} intercalation into the chevrel electrode.

Using quantitative solid-state ^{27}Al NMR measurements, we previously established that Al^{3+} cations intercalate "simultaneously" into cavities 1 and 2 of chevrel Mo_6S_8,[15] as opposed to sequentially as observed for Mg^{2+} cations,[25] consistent with XRD analyses of Geng et al.[24] Al^{3+} cations intercalate into cavity 1, but due to strong Coulombic repulsions among them, the ions "hop" into cavity 2 before cavity 1 is filled. This movement of ions is due to strong cation−cation repulsion and results in an additional CV peak with reduced overpotential, as discussed previously.[15] However, in chevrel Mo_6Se_8, only two CV reduction peaks are observed, while the length of the first galvanostatic discharge plateau is ∼75% of the total specific capacity, suggesting that Al^{3+} cations intercalate sequentially into cavities 1 and 2 during the first and second discharge plateaus, respectively. This Al-ion intercalation mechanism is consistent with reduced cation−cation repulsions among intercalated Al^{3+} cations, which are screened by the larger Se atoms, as well as the more facile diffusion of Al^{3+} cations within the chevrel Mo_6Se_8. In addition, the potential differences ΔE between the first CV reduction peak (0.34 V) and its corresponding coupled oxidation peak (0.47 V) are much less in Mo_6Se_8 (0.13 V) compared to Mo_6S_8 (0.22 V), further suggesting a lower activation barrier for ion diffusion.

To measure the solid-state diffusion of Al^{3+} cations within the chevrel frameworks and the equilibrium potentials at which intercalation occurs, galvanostatic intermittent titration technique (GITT) measurements were performed on Al−Mo_6Se_8 and Al−Mo_6S_8 cells (Figure 1c). Al^{3+} cation diffusion coefficients during the first discharge plateau, which occurs at an equlibrium potential of 0.60 V for Mo_6S_8 and 0.40 V for Mo_6Se_8, were on the order of 10^{-19} and 10^{-17} cm^2/s, respectively (Text S1, Supporting Information). Al^{3+} cation diffusion within Mo_6Se_8 is approximately two orders-of-magnitude faster compared to Mo_6S_8 during the first discharge voltage plateau. Faster cation diffusion is attributed to (i) the higher electronic polarizability of the anionic selenium framework[18] and (ii) the larger size of Se, which reduces cation−cation interactions between intercalated Al^{3+} and the Mo_6 octahedra, resulting in lower activation energies for ion hopping between cavities. Note that a similar trend has also been observed in other transition metal chalcogenides, such as the magnesium spinels MgX_2Z_4 (Z = S, Se; X = In, Y, Sc)[45] and the rare earth spinels $MgLn_2X_4$ (Ln = lanthanide; X = S, Se),[46] where the higher electronic polarizability of the chalcogen network reduces the activation energy for cation migration.[47]

The thermodynamic intercalation potentials computed using strongly constrained and appropriately normed semilocal (SCAN) density functionals[40] (Figure 1c) match well with the experimental potentials. Note that the DFT-predicted voltage represents the average potentials for Al intercalation, resulting in the step-like nature of the calculated voltage curve.

Electron Charge Transfer Mechanism. Solid-state NMR spectroscopy is highly sensitive to electronic environments at the atomic scale; thus, the electrochemical reduction of the chevrel framework, i.e., the addition of electrons required to charge balance Al^{3+} cation insertion, is expected to result in observable NMR shifts. To measure changes in the electronic structure of the chevrel framework, solid-state ^{77}Se and ^{95}Mo NMR spectra were acquired on pristine Mo_6Se_8 and electrochemically discharged $Al_{4/3}Mo_6Se_8$ electrodes. Solid-state ^{77}Se MAS NMR measurements performed on pristine Mo_6Se_8 revealed two Knight-shifted[48,49] ^{77}Se signals with isotropic shifts of 3565 and 2739 ppm and broad spinning-side-band manifolds (Figure 2a). Spectral deconvolutions of both the ^{77}Se MAS and static NMR spectra (Figure 2b) enabled the relative populations of selenium atoms in each site to be quantified and their ^{77}Se NMR parameters to be determined, including isotropic shifts and shift anisotropy

https://doi.org/10.1021/jacs.3c02542
J. Am. Chem. Soc. 2023, 145, 15816−15826

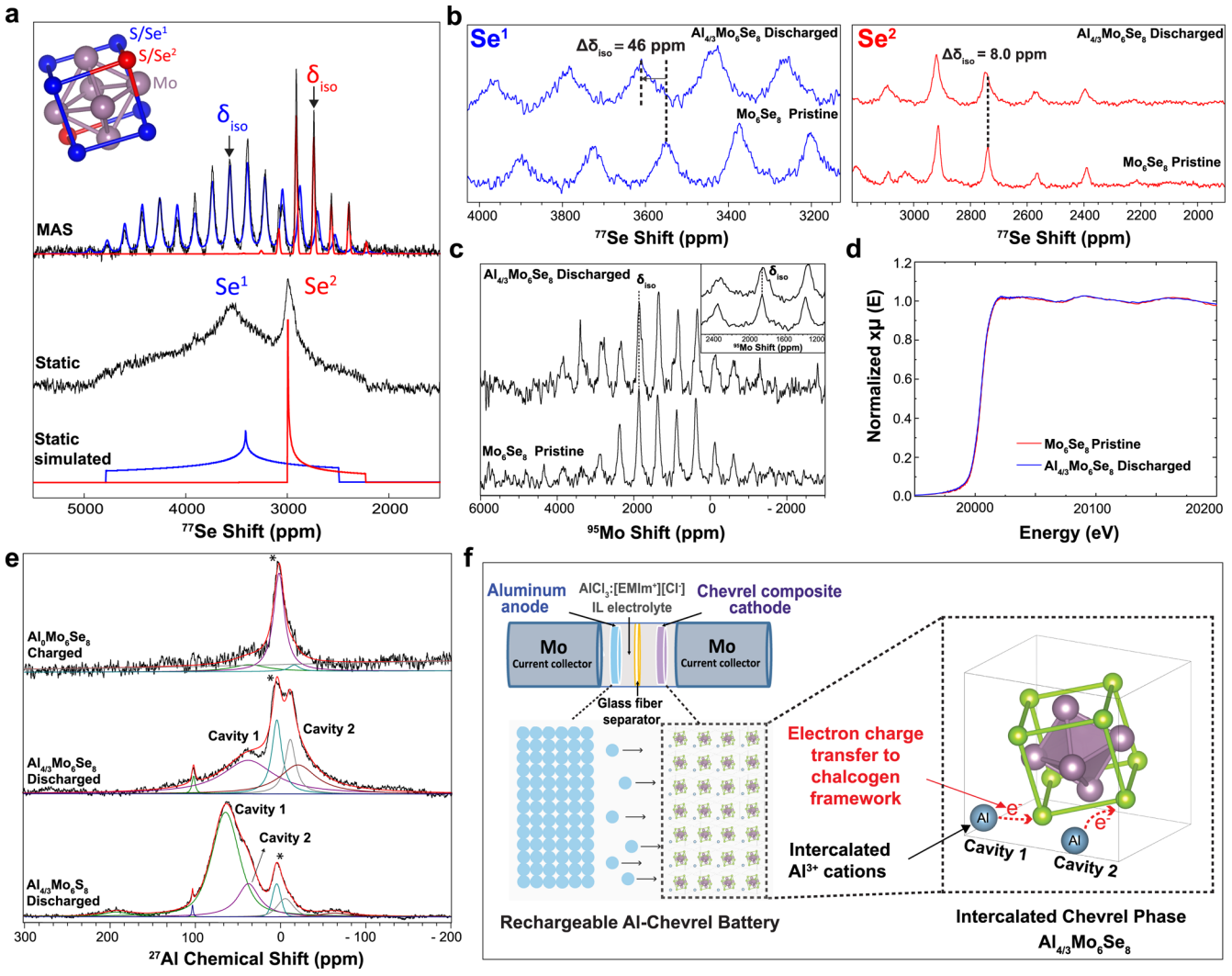

Figure 2. Experimental observation of the electron charge storage mechanism. (a) Solid-state ^{77}Se MAS NMR measurements acquired on pristine Mo_6Se_8 (black) with deconvolutions of crystallographic Se^1 (blue) and Se^2 (red) sites. Inset: molecular structure of Mo_6Se_8 (Se^1: blue, Se^2: red, Mo: purple). The experimental and simulated static ^{77}Se NMR spectra of pristine Mo_6Se_8 are shown below the MAS spectrum. (b) Solid-state ^{77}Se NMR spectra of pristine Mo_6Se_8 and discharged $Al_{4/3}Mo_6Se_8$ electrodes, highlighting the Se^1 region (left, blue) and Se^2 region (right, red). (c) Solid-state ^{95}Mo NMR on pristine Mo_6Se_8 and discharged $Al_{4/3}Mo_6Se_8$ electrodes. Inset: region with isotropic ^{95}Mo shift. (d) Synchrotron XANES measurement of the Mo K-edge for pristine Mo_6Se_8 and discharged $Al_{4/3}Mo_6Se_8$ electrodes. (e) Solid-state ^{27}Al NMR spectra for discharged $Al_{4/3}Mo_6S_8$, discharged $Al_{4/3}Mo_6Se_8$. Asterisks (*) denote insoluble surface species. All NMR measurements were performed at 20 kHz MAS and 14.1 T. (f) Schematic of electrochemical intercalation of Al^{3+} cations and electron transfer.

tensorial parameters associated with the atomic-level electronic environment (Table S1), enabling ^{77}Se signal assignments. The ^{77}Se signal with an isotropic shift of 3565 ppm is attributed to selenium atoms in the six "peripheral" 4-coordinated Se^1 crystallographic sites, consistent with their 75% relative population and anisotropy (asymmetry parameter η of 0.75). The ^{77}Se signal with an isotropic shift at 2739 ppm corresponds to selenium atoms in the two "axial" 3-coordinated Se^2 crystallographic sites, consistent with their 25% population and axial asymmetry (η of 0).[50,51] The large ^{77}Se NMR shifts and anisotropies are dominated by NMR Knight shift effects, which are observed due to the metallic nature of the chevrel phase[44,48,50] and arise from hyperfine couplings between electron spins in the conduction band and nuclear spins. The Knight shift K is described by

$$K = (8\pi/3)\chi_p P_F \quad (4)$$

where χ_p is the Pauli spin susceptibility per atom and P_F is the average value of the s-electron probability density at the Fermi energy E_F.[48,50] Nuclear spins are thus indirect probes of electron spin density within the conduction band.[50] Consequently, the addition of electrons upon electrochemical reduction is expected to result in an increase in the NMR Knight shift and hence the NMR frequency. Note that the Knight shift is a larger interaction than the chemical shift, which is a diamagnetic effect wherein additional electron density increases nuclear shielding and thus decreases the chemical shift and NMR frequency.

Solid-state ^{77}Se MAS NMR measurements were performed on pristine Mo_6Se_8 and discharged $Al_{4/3}Mo_6Se_8$ electrodes to measure electronic changes upon electrochemical Al-ion intercalation (Figure 2b). Notably, the isotropic ^{77}Se shift associated with Se^1 sites increased by 46 ppm upon Al^{3+} intercalation and concomitant reduction of the chevrel framework, a result of an enhanced Knight shift due to

https://doi.org/10.1021/jacs.3c02542
J. Am. Chem. Soc. 2023, 145, 15816−15826

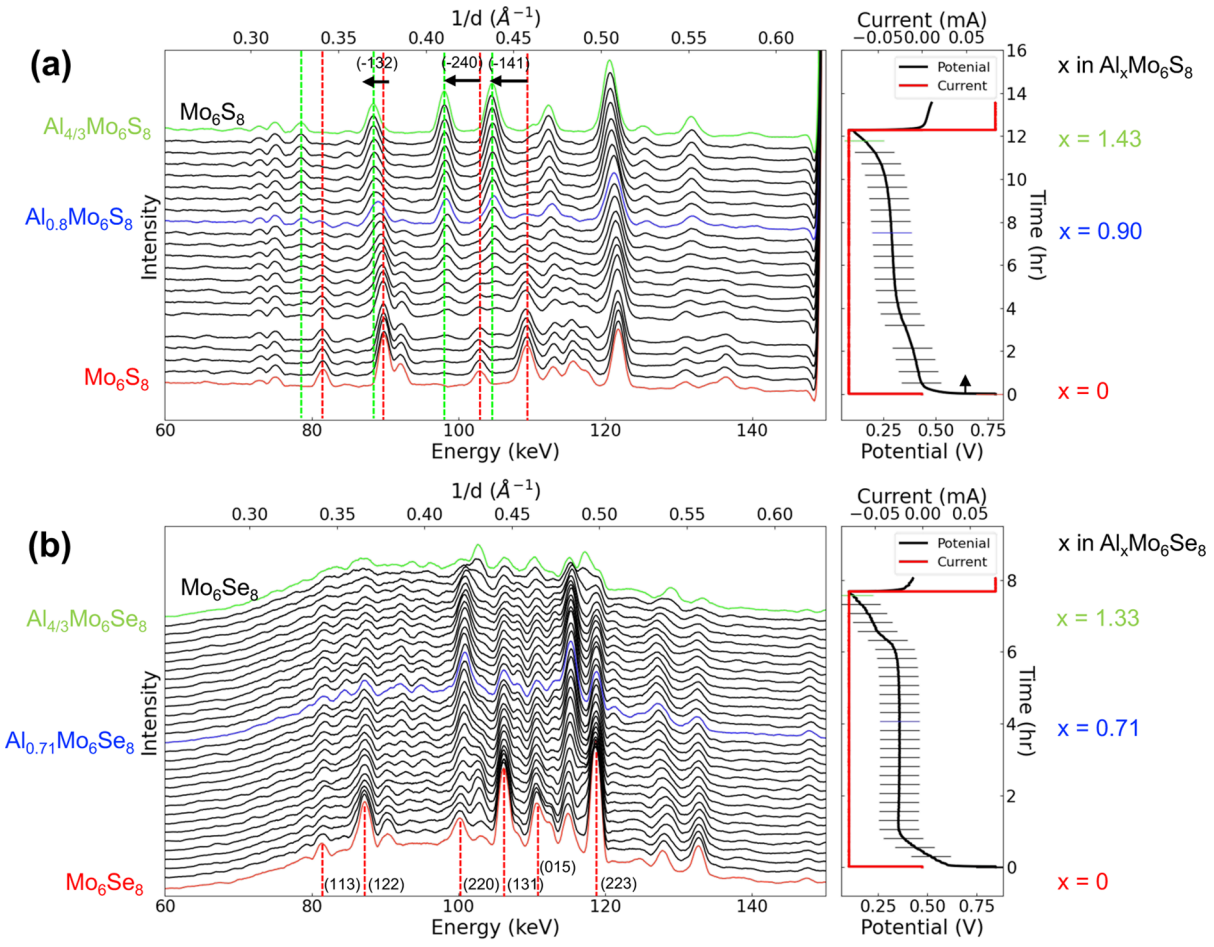

Figure 3. Operando synchrotron EDXRD of Al-chevrel batteries. EDXRD patterns of (a) Al–Mo$_6$S$_8$ and (b) Al–Mo$_6$Se$_8$ cells during first galvanostatic discharge using specific currents of 12 and 8.3 mA/g, respectively. Photon energies and, consequently, $1/d$ values are shown on the bottom and top horizontal axes, respectively.

increased electron density (eq 4) in the anionic chalcogen framework. The ^{77}Se shift associated with Se^2 sites shifted by 8 ppm, indicating a modest increase in electron density. Note that volume expansion and distortion of the Mo$_6$Se$_8$ unit cells also occur upon Al-ion intercalation. The electrochemical intercalation of Al^{3+} into Mo$_6$Se$_8$ alters its electronic structure significantly, as manifested experimentally by the large reduction in drive pressure (ca. 1 bar) needed to spin Al$_{4/3}$Mo$_6$Se$_8$ at 20 kHz MAS and 14.1 T compared to pristine Mo$_6$Se$_8$. Because a conducting sample experiences strong eddy currents when rotated in a magnetic field, resulting in additional forces,[52] this observation is consistent with a decrease in the electrical conductivity of Mo$_6$Se$_8$ upon Al^{3+} intercalation.

To measure changes in the electronic structure of the transition metal Mo$_6$ clusters upon Al-ion intercalation, both solid-state ^{95}Mo MAS NMR and synchrotron Mo K-edge XANES measurements were performed on Mo$_6$Se$_8$ and discharged Al$_{4/3}$Mo$_6$Se$_8$ electrodes. The solid-state single-pulse ^{95}Mo NMR spectra establish one Knight-shifted signal with an isotropic ^{95}Mo shift of 1859 ppm associated with the Mo$_6$ octahedral clusters, which notably do not shift upon Al^{3+} cation intercalation (Figure 2c). Note that ^{95}Mo is an insensitive nucleus due to its low gyromagnetic ratio and quadrupolar nature (spin = 5/2). Synchrotron Mo K-edge XANES measurements at pristine and discharged states were essentially identical, further establishing no change in the oxidation state of the Mo$_6$ clusters upon Al^{3+} intercalation into chevrel phase Mo$_6$Se$_8$ (Figure 2d). Remarkably, the solid-state NMR and XANES measurements establish that the Mo$_6$ clusters remain relatively electronically isolated upon Al^{3+} cation intercalation. Thus, upon electrochemical Al^{3+} intercalation, electrons are transferred directly to the redox active chalcogen frameworks, while the transition metal clusters are redox inactive, establishing that the chevrel phases store charge by reversible electrochemical anionic redox.

To investigate the Al-ion intercalation mechanism, solid-state ^{27}Al single-pulse MAS NMR measurements were acquired under quantitative conditions on the fully intercalated chevrel phase Al$_{4/3}$Mo$_6$Se$_8$ and compared with Al$_{4/3}$Mo$_6$S$_8$, revealing inherent differences in their structural and electronic properties (Figure 2e). In Al$_{4/3}$Mo$_6$Se$_8$, two ^{27}Al signals with shifts of 38 ppm and −10 ppm are associated Al ions within cavities 1 and 2, respectively. The relative populations of Al in cavities 1 and 2, determined by the relative integrated signal intensities, are 74 and 26%, respectively, consistent with the expected compositions. In Al$_{4/3}$Mo$_6$S$_8$, the ^{27}Al shifts of 62 and 38 ppm, associated with tetrahedral aluminum environments, exhibit relative populations of 78 and 22% for cavity 1 and cavity 2, respectively. However, in Al$_{4/3}$Mo$_6$Se$_8$, the ^{27}Al NMR shift of −10 ppm indicates that the intercalated Al^{3+} cation in cavity 2 is in an octahedral environment, as opposed to the

https://doi.org/10.1021/jacs.3c02542
J. Am. Chem. Soc. 2023, 145, 15816−15826

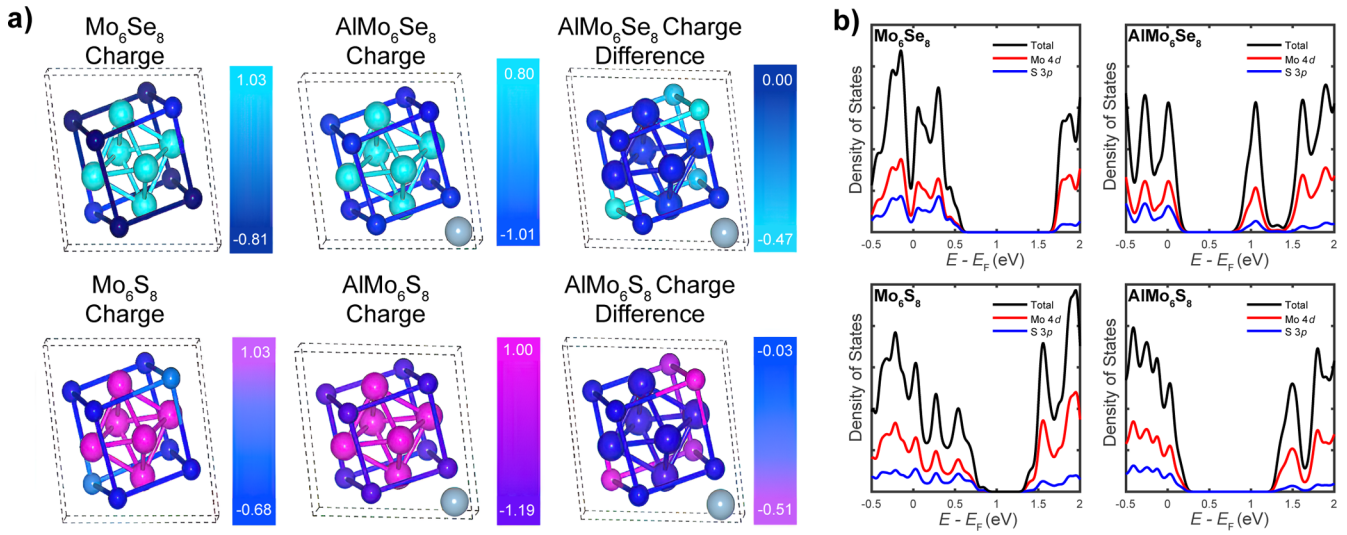

Figure 4. Electron charge transfer mechanism revealed by DFT calculations. (a) Bader charge analysis performed on chevrel Mo_6S_8, Mo_6Se_8, $AlMo_6S_8$, and $AlMo_6Se_8$ unit cell structures. Note that all color bars feature a unique range. The charge difference between the Al-ion intercalated and unintercalated chevrel phases is also shown. (b) Total DOS and PDOS for the chevrel systems.

tetrahedral environments observed for cavity 1 or for both cavities in Mo_6S_8, which was proposed as a possible intercalation site for Mg^{2+} by Levi and Aurbach.[18] Also, the ^{27}Al signals associated with intercalated Al^{3+} cations in cavities 1 and 2 for $Al_{4/3}Mo_6Se_8$ are broader than those for $Al_{4/3}Mo_6S_8$. The Al^{3+} ions "hop" between the six energetically crystallographic sites within each cavity of the chevrel phases, resulting in fast electric quadrupolar relaxation (5 times T_2* <400 μs). Circular ion hopping within a cavity is expected to be faster for Mo_6Se_8 compared to Mo_6S_8, based on the GITT diffusion measurements above. Such faster motions would manifest themselves in faster transverse NMR relaxation times and hence broader ^{27}Al linewidths, as measured here. In addition, solid-state ^{27}Al NMR measurements on the charged Mo_6Se_8 electrode revealed the majority of the aluminum is removed upon de-intercalation with minimal Al-ion trapping (<4%, compared with <7% for Mo_6S_8),[15] highlighting the reversibility of Al-ion intercalation into chevrel Mo_6Se_8.

Crystal Structure Evolution. Operando synchrotron EDXRD measurements were performed to measure how the chevrel Mo_6Se_8 and Mo_6S_8 crystalline structures evolved during electrochemical Al^{3+} intercalation (Figure 3).[53,54] Diffraction data were collected using batteries constructed in hermetically sealed gold-plated CR2032 coin cells without transparent windows or other modifications. As previously reported, the electrochemically intercalated chevrel phases are very sensitive to air;[21] thus, operando characterization was performed to prevent undesired side reactions. In the EDXRD pattern of Al−Mo_6S_8 cells (Figure 3a), the 90 and 103 keV peaks, previously indexed to (−132) and (−240) reflections by Lee et al.,[13] shifted to lower energies during discharge, corresponding to larger *d*-spacings. Rather than a continuous change in *d*-spacing, the transition was discontinuous. This shift to lower energies reveals the expansion of the chevrel $R\bar{3}$ unit cell due to the electrochemical intercalation of Al^{3+} cations. These results agreed with Lee et al.,[13] where there was no transformation in crystal structure as Mo_6S_8 maintained its $R\bar{3}$ space group during Al^{3+} cation insertion. Assuming a final intercalated (discharged) state of $Al_{4/3}Mo_6S_8$, the final calculated discharge product corresponded to $Al_xMo_6S_8$ with x = 1.43, indicating that electrolyte decomposition during the initial part of the galvanostatic discharge accounted for the remaining capacity (x = 0.1, indicated as an arrow on the discharge curve).

In contrast, the EDXRD pattern of Al−Mo_6Se_8 cells (Figure 3b) resulted in a triclinic distortion upon the electrochemical intercalation of Al^{3+} cations and consequently an altered diffraction pattern. Levi et al. have shown that upon electrochemical insertion of Mg^{2+} into Mo_6Se_8, the rhombohedral $R\bar{3}$ structure is distorted to triclinic $P\bar{1}$.[17,18] This result is supported by solid-state ^{27}Al NMR measurements (Figure 2e), wherein cavity 1 of $Al_{4/3}Mo_6Se_8$ is in an octahedral environment, while for $Al_{4/3}Mo_6S_8$, Al^{3+} cations in both cavities are tetrahedrally coordinated. For $Al_{4/3}Mo_6Se_8$, the fully discharged diffraction pattern was not indexed but is similar to patterns reported for $Mg_xMo_6Se_8$ (x = 1, 2) reported by Levi et al.,[17] which exhibit a series of prominent reflections from 110 to 120 keV. Interestingly, several prominent reflections in the discharged material form only in the final moments of discharge, whereupon the final intercalated (discharged) state of $Al_{4/3}Mo_6Se_8$ is obtained. Overall, the synchrotron diffraction results establish that the bonding structure and topology of the crystalline chevrel frameworks are preserved upon electrochemical cycling. Critically, the chevrel phase undergoes reversible anionic redox without the breaking or forming of chemical bonds, unlike some oxygen anionic redox processes that can occur in transition metal oxides, which explains its high electrochemical reversibility.

Calculated Electron Charge Distributions. The electron charge transfer mechanism was further investigated theoretically by DFT calculations (Figure 4). Bader charge analysis (Figure 4a) was performed on Mo_6S_8, Mo_6Se_8, $AlMo_6S_8$, and $AlMo_6Se_8$ unit cell structures to evaluate the spatial distributions of electrons around each atom before and after Al^{3+} cation intercalation (see Table S2 for average charge values for each type of atom). The charge differences between the intercalated and unintercalated chevrel phases establish that electrons are primarily transferred to the anionic chalcogen framework, as opposed to the transition metals. This result corroborates the anionic redox electron charge

https://doi.org/10.1021/jacs.3c02542
J. Am. Chem. Soc. 2023, 145, 15816−15826

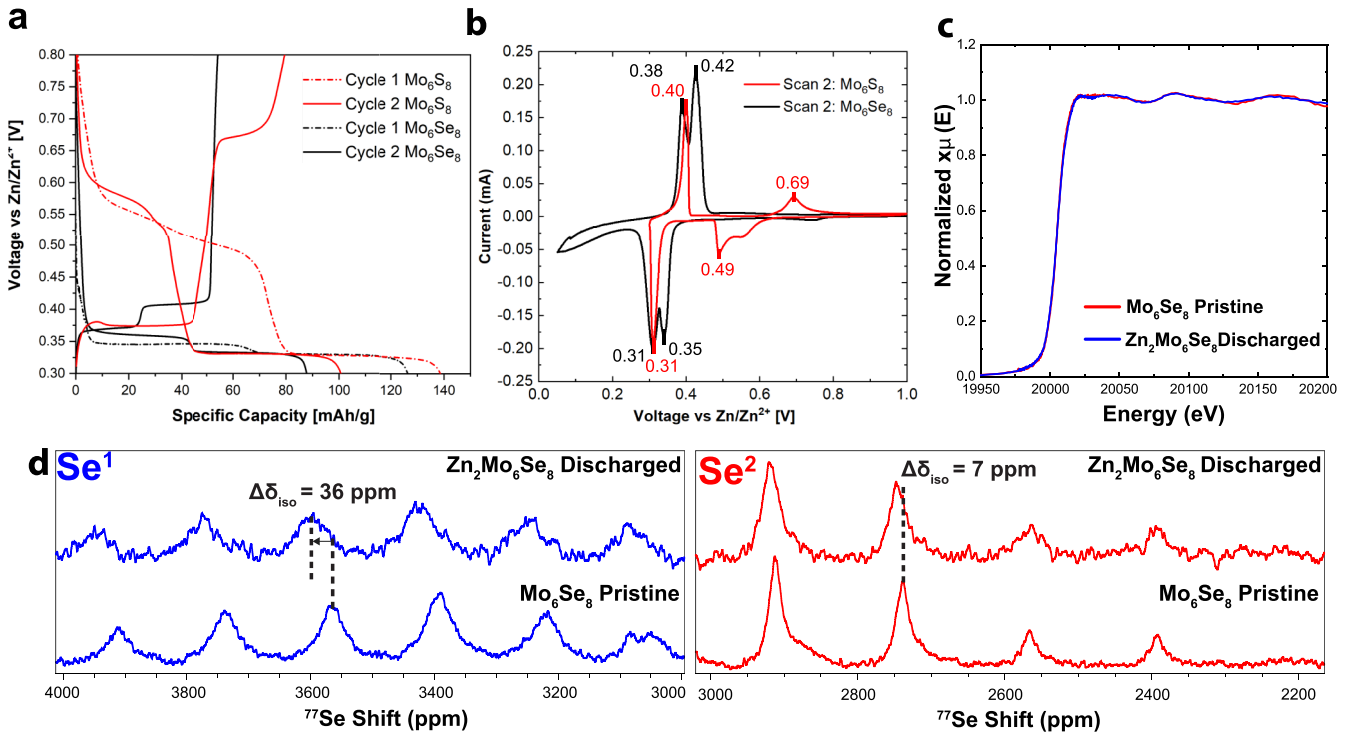

Figure 5. Generalization of the electron charge storage mechanism to the aqueous Zn-chevrel battery system: (a) Galvanostatic cycling (10 mA/g) and (b) CV (50 μV/s, scan 2) of Zn−Mo_6S_8 (red) and Zn−Mo_6Se_8 (black) cells performed at 25 °C. (c) Synchrotron XANES measurements of the Mo K-edge of pristine Mo_6Se_8 and discharged $Zn_2Mo_6Se_8$ electrodes. (d) Solid-state ^{77}Se MAS NMR spectra of pristine Mo_6Se_8 and discharged $Zn_2Mo_6Se_8$ electrodes, highlighting the Se^1 region (left, blue) and Se^2 region (right, red).

transfer mechanism measured experimentally by solid-state NMR spectroscopy and XANES. The DFT results show that two characteristic types of chalcogen atoms exist, consistent with the Se^1 and Se^2 measured by solid-state ^{77}Se NMR (Figure 2a). Crucially, the DFT results also indicate that the electron charge transfer mechanism observed experimentally for chevrel Mo_6Se_8 also pertains to chevrel Mo_6S_8, which was challenging to characterize experimentally using analogous spectroscopic methods. Thus, the anionic redox mechanism observed in the chevrel phases does not appear to be dependent upon the type of chalcogen atom present within the anionic framework.

The total density of states (DOS) was also calculated for the chevrel systems (Figure 4b, black; see Figure S2 for overlayed spectra). The results indicate that all materials are metallic, based on their states being present at the Fermi level (E_F). Chevrel Mo_6Se_8 systems maintained a larger bandgap than chevrel Mo_6S_8 systems, independent of Al^{3+} cation insertion. Additionally, the projected DOSs (PDOS) are shown for the Mo 4d orbitals (Figure 4b, red) and the S or Se 3p orbitals (Figure 4b, blue). The unoccupied states accept the electrons upon electrochemical reduction and Al^{3+} cation intercalation, causing the PDOS spectra to shift to lower energies. This calculation is consistent with the change in Knight shift observed in solid-state ^{77}Se NMR measurements (Figure 2b), as well as the indirect observation of the change in conductivity of the chevrel samples upon Al^{3+} intercalation, as discussed above.

Generality of the Electron Charge Storage Mechanism. To further probe the generality of the electron charge storage mechanism, divalent Zn^{2+} cations were electrochemically intercalated into Mo_6Se_8 electrodes for the first time, and similar spectroscopic measurements were performed to elucidate changes in electronic structure (Figure 5). Zinc metal was used as the anode and aqueous 1 M $Zn(SO_4)$ was used as the electrolyte. Galvanostatic cycling (Figure 5a) of the Zn−Mo_6Se_8 cell, with Zn−Mo_6S_8 cells shown for comparison, reveals two distinct discharge plateaus that achieve the theoretical capacities of 88 and 128 mA h/g upon full discharge, respectively, corresponding to $Zn_2Mo_6Se_8$ and $Zn_2Mo_6S_8$. CV (Figure 5b) reveals two distinct reduction peaks at 0.35 and 0.31 V for Mo_6Se_8 and 0.49 and 0.31 V for Mo_6S_8. Synchrotron XANES measurements of the Mo K-edge of pristine Mo_6Se_8 and discharged $Zn_2Mo_6Se_8$ states (Figure 5c) were identical, indicating that the transition metal Mo_6 octahedra are redox inactive. Solid-state ^{77}Se NMR experiments (Figure 5d) reveal that the isotropic ^{77}Se NMR signals shift to more positive frequencies upon electrochemical intercalation of Zn^{2+} cations, consistent with increased electron density as per the Knight shift effect (eq 4). As upon Al^{3+} intercalation, the majority of electrons are transferred specifically to the 4-coordinated Se^1 atoms (^{77}Se shift of 36 ppm) upon Zn^{2+} intercalation, with a more modest quantity transferred to the 3-coordinated Se^2 atoms (^{77}Se shift of 7 ppm). Thus, an identical anionic redox electron charge transfer mechanism occurs when multivalent cations with different valences and coulombic charge densities (Al^{3+}, Zn^{2+}) electrochemically intercalate within the chevrel Mo_6Se_8 framework. In aggregate, these results are also consistent and build upon with the work of Thole et al.[22] and Wan et al.,[23] whose work indicates that in chevrel Mo_6S_8 only the sulfur framework participates in electron charge transfer upon divalent Mg^{2+} cation insertion.

Operando synchrotron EDXRD patterns of Zn−Mo_6S_8 and Zn−Mo_6Se_8 cells (Figure S3) revealed that intermediate $ZnMo_6S_8$ and $ZnMo_6Se_8$ phases formed during discharge,

https://doi.org/10.1021/jacs.3c02542
J. Am. Chem. Soc. 2023, 145, 15816−15826

respectively, ending in distinct $Zn_2Mo_6S_8$ and $Zn_2Mo_6Se_8$ phases. The Zn−Mo_6S_8 cell showed a well-defined transition from Mo_6S_8 to a $ZnMo_6S_8$ phase at $Zn_xMo_6S_8$ with $x = 0.98$ ($x \approx 1$), where coexistence of both phases appeared over a range of x-values and an equivalence between the two phases occurred at $x = 0.53$. A similar conversion of the $ZnMo_6S_8$ phase to the $Zn_2Mo_6S_8$ phase occurs with an equivalence between phases occurring at $x = 1.66$. A comparison of the operando synchrotron EDXRD patterns of the Zn−Mo_6S_8 and Al−Mo_6S_8 cells (Figure S4) highlights that the $Zn_xMo_6S_8$ system has three distinct phases, compared to only two for the $Al_xMo_6S_8$ system, a consequence of the different ion valences and quantities intercalated (2 for Zn^{2+} vs 4/3 and Al^{3+}) per Mo_6S_8 unit. Overall, as with Al^{3+} cation intercalation, the bonding structure and topology of the crystalline chevrel frameworks were preserved upon Zn^{2+} cation intercalation.

CONCLUSIONS

Using the electrochemical intercalation of Al^{3+} and Zn^{2+} cations into chevrel Mo_6Se_8 and Mo_6S_8 electrodes as model battery systems, we elucidate experimentally and theoretically that the chevrel phase undergoes reversible electrochemical anionic redox as an electronic charge storage mechanism. The anionic redox occurs without breaking or forming chemical bonds, preserving the crystal structure and explaining the high degree of electrochemical reversibility. In contrast, the transition metal octahedra are redox inactive. This electronic charge storage mechanism is fundamentally different than that observed for the majority of intercalation battery electrodes, wherein the transition metals are redox active. In addition, the nature of the anionic redox phenomenon is different than that observed in lithium-rich transition metal oxides and chalcogenides, which couple cationic and anionic redox processes, are a result of excess lithium, and often result in electrode instabilities and capacity fade. The results also yield insights into how cation-framework and cation−cation interactions affect the intercalation mechanism of multivalent ions within chevrel-phase electrodes.

We propose that reversible electrochemical anionic redox may be incorporated as a potential material design principle for future multivalent intercalation electrodes, which must not only electrochemically intercalate multivalent cations but also enable those high-charge-density cations to diffuse through their structures. With regards to ion diffusion, the chevrel phases not only have large 3D cavities, but also their electroactive and electronically polarizable anionic frameworks are in close molecular proximity to the intercalated cations and their diffusional transition states between cavities. While chevrel-phase electrodes cannot provide the energy densities necessary for demanding technological applications, computational materials discovery methods using similar anionic redox principles to those elucidated here are worth considering in the search for a multivalent intercalation electrode that is "beyond chevrel". Overall, we hope that this research provides new strategies into the molecular-level design of novel intercalation electrodes for rechargeable multivalent-ion batteries.

ASSOCIATED CONTENT

Supporting Information

The Supporting Information is available free of charge at https://pubs.acs.org/doi/10.1021/jacs.3c02542.

Calculation of Al^{3+} cation diffusion coefficients by GITT measurements; additional galvanostatic cycling and cyclic voltammetry of Al−Mo_6Se_8 cells; solid-state ^{77}Se NMR parameters of chevrel Mo_6Se_8; DFT total DOS calculations and Bader charge analyses of Mo_6Se_8, $AlMo_6Se_8$, Mo_6S_8, and $AlMo_6S_8$; operando synchrotron EDXRD of Zn−Mo_6S_8 and Zn−Mo_6Se_8 cells; and comparison of operando synchrotron EDXRD of Al−Mo_6S_8 and Zn−Mo_6S_8 cells (PDF)

AUTHOR INFORMATION

Corresponding Authors

Joshua W. Gallaway − *Department of Chemical Engineering, Northeastern University, Boston, Massachusetts 02115, United States;* orcid.org/0000-0002-6798-7781; Email: j.gallaway@northeastern.edu

Manuel Smeu − *Department of Physics, Binghamton University, SUNY, Binghamton, New York 13902, United States;* orcid.org/0000-0001-9548-4623; Email: msmeu@binghamton.edu

Robert J. Messinger − *Department of Chemical Engineering, The City College of New York, CUNY, New York, New York 10031, United States;* orcid.org/0000-0002-5537-3870; Email: rmessinger@ccny.cuny.edu

Authors

Ankur L. Jadhav − *Department of Chemical Engineering, The City College of New York, CUNY, New York, New York 10031, United States;* orcid.org/0000-0002-6481-4084

Taylor R. Juran − *Department of Physics, Binghamton University, SUNY, Binghamton, New York 13902, United States;* orcid.org/0000-0002-2441-1918

Matthew A. Kim − *Department of Chemical Engineering, Northeastern University, Boston, Massachusetts 02115, United States*

Andrea M. Bruck − *Department of Chemical Engineering, Northeastern University, Boston, Massachusetts 02115, United States;* orcid.org/0000-0002-2113-066X

Brendan E. Hawkins − *Department of Chemical Engineering, The City College of New York, CUNY, New York, New York 10031, United States;* orcid.org/0000-0001-6238-4239

Complete contact information is available at: https://pubs.acs.org/10.1021/jacs.3c02542

Notes

The authors declare no competing financial interest.

ACKNOWLEDGMENTS

A.L.J., B.E.H., and R.J.M. acknowledge funding from the U.S. National Science Foundation through NSF CAREER award CBET-1847552 and the U.S. National Aeronautics and Space Administration (NASA) via the NASA-CCNY Center for Advanced Batteries for Space under cooperative agreement 80NSSC19M0199. NMR measurements were acquired in the City University of New York (CUNY) Advanced Science Research Center (ASRC) NMR facility. T.R.J. and M.S. acknowledge startup funding from Binghamton University. DFT calculations were performed using the Extreme Science and Engineering Discovery Environment (XSEDE, supported by NSF award ACI-1053575) under allocation TG-DMR180009 and the Binghamton University HPC cluster, "Spiedie". M.A.K., A.M.B., and J.W.G. acknowledge startup

funding from Northeastern University. This research used resources of the Advanced Photon Source; a U.S. Department of Energy (DOE) Office of Science User Facility operated for the DOE Office of Science by Argonne National Laboratory under contract no. DE-AC02-06CH11357. This research also used resources at beamline 7-BM (QAS) of the National Synchrotron Light Source II, a U.S. DOE Office of Science User Facility operated for the DOE Office of Science by Brookhaven National Laboratory under contract no. DE-SC0012704.

REFERENCES

(1) Goodenough, J. B.; Park, K. S. The Li-Ion Rechargeable Battery: A Perspective. *J. Am. Chem. Soc.* **2013**, *135*, 1167−1176.
(2) Muldoon, J.; Bucur, C. B.; Gregory, T. Quest for Nonaqueous Multivalent Secondary Batteries: Magnesium and Beyond. *Chem. Rev.* **2014**, *114*, 11683−11720.
(3) Canepa, P.; Sai Gautam, G.; Hannah, D. C.; Malik, R.; Liu, M.; Gallagher, K. G.; Persson, K. A.; Ceder, G. Odyssey of Multivalent Cathode Materials: Open Questions and Future Challenges. *Chem. Rev.* **2017**, *117*, 4287−4341.
(4) Chen, R.; Luo, R.; Huang, Y.; Wu, F.; Li, L. Advanced High Energy Density Secondary Batteries with Multi-Electron Reaction Materials. *Adv. Sci.* **2016**, *3*, 1600051.
(5) Guduru, R. K.; Icaza, J. C. A Brief Review on Multivalent Intercalation Batteries with Aqueous Electrolytes. *Nanomaterials* **2016**, *6*, 41.
(6) Aurbach, D.; Lu, Z.; Schechter, A.; Gofer, Y.; Gizbar, H.; Turgeman, R.; Cohen, Y.; Moshkovich, M.; Levi, E. Prototype Systems for Rechargeable Magnesium Batteries. *Nature* **2000**, *407*, 724−727.
(7) Linden, D.; Reddy, T. B. *Handbook of Batteries*; McGraw-Hill, 2002.
(8) Geng, L.; Lv, G.; Xing, X.; Guo, J. Reversible Electrochemical Intercalation of Aluminum in Mo_6S_8. *Chem. Mater.* **2015**, *27*, 4926−4929.
(9) Chae, M. S.; Hong, S. T. Prototype System of Rocking-Chair Zn-Ion Battery Adopting Zinc Chevrel Phase Anode and Rhombohedral Zinc Hexacyanoferrate Cathode. *Batteries* **2019**, *5*, 3.
(10) Tarascon, J. M.; Hull, G. W.; Marsh, P.; Haar, T. Electrochemical, Structural, and Physical Properties of the Sodium Chevrel Phases $Na_xMo_6X_{8-Y}I_y$ (X = S, Se and y = 0 to 2). *J. Solid State Chem.* **1987**, *66*, 204−224.
(11) Aselmann, G.; Müller-Warmuth, W.; Gocke, E.; Schöllhorn, R. ^{7}Li NMR Studies in Chevrel Phases $Li_xMo_6X_8$. *Z. Phys. Chem.* **1987**, *151*, 103−111.
(12) Cheng, Y.; Luo, L.; Zhong, L.; Chen, J.; Li, B.; Wang, W.; Mao, S. X.; Wang, C.; Sprenkle, V. L.; Li, G.; Liu, J. Highly Reversible Zinc-Ion Intercalation into Chevrel Phase Mo_6S_8 Nanocubes and Applications for Advanced Zinc-Ion Batteries. *ACS Appl. Mater. Interfaces* **2016**, *8*, 13673−13677.
(13) Lee, B.; Lee, H. R.; Yim, T.; Kim, J. H.; Lee, J. G.; Chung, K. Y.; Cho, B. W.; Oh, S. H. Investigation on the Structural Evolutions during the Insertion of Aluminum Ions into Mo_6S_8 Chevrel Phase. *J. Electrochem. Soc.* **2016**, *163*, A1070−A1076.
(14) Juran, T. R.; Smeu, M. Hybrid Density Functional Theory Modeling of Ca, Zn, and Al Ion Batteries Using the Chevrel Phase Mo_6S_8 Cathode. *Phys. Chem. Chem. Phys.* **2017**, *19*, 20684−20690.
(15) Jadhav, A. L.; Xu, J. H.; Messinger, R. J. Quantitative Molecular-Level Understanding of Electrochemical Aluminum-Ion Intercalation into a Crystalline Battery Electrode. *ACS Energy Lett.* **2020**, *5*, 2842−2848.
(16) Chevrel, R.; Sergent, M.; Prigent, J. Sur de Nouvelles Phases Sulfurées Ternaires Du Molybdène. *J. Solid State Chem.* **1971**, *3*, 515−519.
(17) Levi, E.; Mitelman, A.; Isnard, O.; Brunelli, M.; Aurbach, D. Phase Diagram of Mg Insertion into Chevrel Phases, $Mg_xMo_6T_8$ (T = S, Se). 3. The Crystal Structure of Triclinic $Mg_2Mo_6Se_8$. *Inorg. Chem.* **2008**, *47*, 1975−1983.
(18) Levi, E.; Aurbach, D. Chevrel Phases, $M_xMo_6T_8$ (M = Metals, T = S, Se, Te) as a Structural Chameleon: Changes in the Rhombohedral Framework and Triclinic Distortion. *Chem. Mater.* **2010**, *22*, 3678−3692.
(19) Durham, J. L.; Wilson, W. B.; Huh, D. N.; McDonald, R.; Szczepura, L. F. Organometallic Rhenium (III) Chalcogenide Clusters: Coordination of N-Heterocyclic Carbenes. *Chem. Commun.* **2015**, *51*, 10536−10538.
(20) Bruck, A. M.; Yin, J.; Tong, X.; Takeuchi, E. S.; Takeuchi, K. J.; Szczepura, L. F.; Marschilok, A. C. Reversible Electrochemical Lithium-Ion Insertion into the Rhenium Cluster Chalcogenide−Halide $Re_6Se_8Cl_2$. *Inorg. Chem.* **2018**, *57*, 4812−4815.
(21) Richard, J.; Benayad, A.; Colin, J. F.; Martinet, S. Charge Transfer Mechanism into the Chevrel Phase Mo_6S_8 during Mg Intercalation. *J. Phys. Chem. C* **2017**, *121*, 17096−17103.
(22) Thöle, F.; Wan, L. F.; Prendergast, D. Re-Examining the Chevrel Phase Mo_6S_8 cathode for Mg Intercalation from an Electronic Structure Perspective. *Phys. Chem. Chem. Phys.* **2015**, *17*, 22548−22551.
(23) Wan, L. F.; Wright, J.; Perdue, B. R.; Fister, T. T.; Kim, S.; Apblett, C. A.; Prendergast, D. Revealing Electronic Structure Changes in Chevrel Phase Cathodes upon Mg Insertion Using X-Ray Absorption Spectroscopy. *Phys. Chem. Chem. Phys.* **2016**, *18*, 17326−17329.
(24) Geng, L.; Scheifers, J. P.; Zhang, J.; Bozhilov, K. N.; Fokwa, B. P. T.; Guo, J. Crystal Structure Transformation in Chevrel Phase Mo_6S_8 Induced by Aluminum Intercalation. *Chem. Mater.* **2018**, *30*, 8420−8425.
(25) Levi, E.; Lancry, E.; Mitelman, A.; Aurbach, D.; Ceder, G.; Morgan, D.; Isnard, O. Phase Diagram of Mg Insertion into Chevrel Phases, $Mg_xMo_6T_8$ (T = S, Se). 1. Crystal Structure of the Sulfides. *Chem. Mater.* **2006**, *18*, 5492−5503.
(26) Thackeray, M. M.; David, W. I. F.; Bruce, P. G.; Goodenough, J. B. Lithium Insertion into Manganese Spinels. *Mater. Res. Bull.* **1983**, *18*, 461−472.
(27) Sathiya, M.; Rousse, G.; Ramesha, K.; Laisa, C. P.; Vezin, H.; Sougrati, M. T.; Doublet, M. L.; Foix, D.; Gonbeau, D.; Walker, W.; Prakash, A. S.; ben Hassine, M.; Dupont, L.; Tarascon, J. M. Reversible Anionic Redox Chemistry in High-Capacity Layered-Oxide Electrodes. *Nat. Mater.* **2013**, *12*, 827−835.
(28) ben Yahia, M.; Vergnet, J.; Saubanère, M.; Doublet, M. L. Unified Picture of Anionic Redox in Li/Na-Ion Batteries. *Nat. Mater.* **2019**, *18*, 496−502.
(29) Assat, G.; Tarascon, J. M. Fundamental Understanding and Practical Challenges of Anionic Redox Activity in Li-Ion Batteries. *Nat. Energy* **2018**, *3*, 373−386.
(30) Assat, G.; Iadecola, A.; Foix, D.; Dedryvere, R.; Tarascon, J. M. Direct Quantification of Anionic Redox over Long Cycling of Li-Rich Nmc via Hard x-Ray Photoemission Spectroscopy. *ACS Energy Lett.* **2018**, *3*, 2721−2728.
(31) Flamary-Mespoulie, F.; Boulineau, A.; Martinez, H.; Suchomel, M. R.; Delmas, C.; Pecquenard, B.; le Cras, F. Lithium-Rich Layered Titanium Sulfides: Cobalt-and Nickel-Free High Capacity Cathode Materials for Lithium-Ion Batteries. *Energy Storage Mater.* **2020**, *26*, 213−222.
(32) Hansen, C. J.; Zak, J. J.; Martinolich, A. J.; Ko, J. S.; Bashian, N. H.; Kaboudvand, F.; van der Ven, A.; Melot, B. C.; Nelson Weker, J.; See, K. A. Multielectron, Cation and Anion Redox in Lithium-Rich Iron Sulfide Cathodes. *J. Am. Chem. Soc.* **2020**, *142*, 6737−6749.
(33) Martinolich, A. J.; Zak, J. J.; Agyeman-Budu, D. N.; Kim, S. S.; Bashian, N. H.; Irshad, A.; Narayan, S. R.; Melot, B. C.; Nelson Weker, J.; See, K. A. Controlling Covalency and Anion Redox Potentials through Anion Substitution in Li-Rich Chalcogenides. *Chem. Mater.* **2020**, *33*, 378−391.
(34) Saha, P.; Jampani, P. H.; Datta, M. K.; Hong, D.; Gattu, B.; Patel, P.; Kadakia, K. S.; Manivannan, A.; Kumta, P. N. A Rapid Solid-State Synthesis of Electrochemically Active Chevrel Phases (Mo_6T_8;

https://doi.org/10.1021/jacs.3c02542
J. Am. Chem. Soc. 2023, 145, 15816−15826

T = S, Se) for Rechargeable Magnesium Batteries. *Nano Res.* **2017**, *10*, 4415−4435.
(35) Massiot, D.; Fayon, F.; Capron, M.; King, I.; le Calvé, S.; Alonso, B.; Durand, J. O.; Bujoli, B.; Gan, Z.; Hoatson, G. Modelling One- and Two-Dimensional Solid-State NMR Spectra. *Magn. Reson. Chem.* **2002**, *40*, 70−76.
(36) Kresse, G.; Hafner, J. Ab Initio Molecular-Dynamics Simulation of the Liquid-Metalamorphous- Semiconductor Transition in Germanium. *Phys. Rev. B: Condens. Matter Mater. Phys.* **1994**, *49*, 14251−14269.
(37) Kresse, G.; Hafner, J. Ab Initio Molecular Dynamics for Liquid Metals. *Phys. Rev. B: Condens. Matter Mater. Phys.* **1993**, *47*, 558−561.
(38) Kresse, G.; Furthmüller, J. Efficient Iterative Schemes for Ab Initio Total-Energy Calculations Using a Plane-Wave Basis Set. *Phys. Rev. B: Condens. Matter Mater. Phys.* **1996**, *54*, 11169−11186.
(39) Blöchl, P. E. Projector Augmented-Wave Method. *Phys. Rev. B: Condens. Matter Mater. Phys.* **1994**, *50*, 17953−17979.
(40) Sun, J.; Remsing, R. C.; Zhang, Y.; Sun, Z.; Ruzsinszky, A.; Peng, H.; Yang, Z.; Paul, A.; Waghmare, U.; Wu, X. SCAN: An Efficient Density Functional Yielding Accurate Structures and Energies of Diversely-Bonded Materials. **2015**, arXiv:1511.01089. arXiv preprint (accessed Feb 21, 2021).
(41) Levi, E.; Lancry, E.; Mitelman, A.; Aurbach, D.; Isnard, O.; Djurado, D. Phase Diagram of Mg Insertion into Chevrel Phases, $Mg_xMo_6T_8$ (T = S, Se). 2. THe Crystal Structure of Triclinic $MgMo_6Se_8$. *Chem. Mater.* **2006**, *18*, 3705−3714.
(42) Smeu, M.; Hossain, M. S.; Wang, Z.; Timoshevskii, V.; Bevan, K. H.; Zaghib, K. Theoretical Investigation of Chevrel Phase Materials for Cathodes Accommodating Ca2+ Ions. *J. Power Sources* **2016**, *306*, 431−436.
(43) Aydinol, M. K.; Ceder, G. First-Principles Prediction of Insertion Potentials in Li-Mn Oxides for Secondary Li Batteries. *J. Electrochem. Soc.* **1997**, *144*, 3832−3835.
(44) Levi, M. D.; Lancri, E.; Levi, E.; Gizbar, H.; Gofer, Y.; Aurbach, D. The Effect of the Anionic Framework of Mo_6X_8 Chevrel Phase (X = S, Se) on the Thermodynamics and the Kinetics of the Electrochemical Insertion of Mg^{2+} Ions. *Solid State Ionics* **2005**, *176*, 1695−1699.
(45) Canepa, P.; Bo, S.-H.; Sai Gautam, G.; Key, B.; Richards, W. D.; Shi, T.; Tian, Y.; Wang, Y.; Li, J.; Ceder, G. High Magnesium Mobility in Ternary Spinel Chalcogenides. *Nat. Commun.* **2017**, *8*, 1759.
(46) Koettgen, J.; Bartel, C. J.; Ceder, G. Computational Investigation of Chalcogenide Spinel Conductors for All-Solid-State Mg Batteries. *Chem. Commun.* **2020**, *56*, 1952−1955.
(47) Bonnick, P.; Blanc, L.; Vajargah, S. H.; Lee, C.-W.; Sun, X.; Balasubramanian, M.; Nazar, L. F. Insights into Mg^{2+} Intercalation in a Zero-Strain Material: Thiospinel $Mg_xZr_2S_4$. *Chem. Mater.* **2018**, *30*, 4683−4693.
(48) Knight, W. D. The Knight Shift. *Philos. Mag. B* **1999**, *79*, 1231−1237.
(49) Hamard, C.; Auffret, V.; Peña, O.; le Floch, M.; Nowak, B.; Wojakowski, A. Chevrel-Phase Solid Solution $Mo_6Se_{8-X}Te_x$. Study of Its Superconducting, Magnetic and NMR Properties. *Phys. B* **2000**, *291*, 339−349.
(50) Bennett, L. H.; Watson, R. E.; Carter, G. C. Relevance of Knight Shift Measurements to the Electronic Density of States. *J. Res. Natl. Bur. Stand. A: Phys. Chem.* **1970**, *74A*, 569.
(51) Hamard, C.; Le Floch, M.; Peña, O.; Wojakowski, A. NMR in Chevrel-Phase Solid Solution $Mo_6Se_{8-X}Te_x$. *Phys. B* **1999**, *259*−*261*, 701−702.
(52) Pecher, O.; Carretero-Gonzalez, J.; Griffith, K. J.; Grey, C. P. Materials' Methods: NMR in Battery Research. *Chem. Mater.* **2017**, *29*, 213−242.
(53) Bruck, A. M.; Kim, M. A.; Ma, L.; Ehrlich, S. N.; Okasinski, J. S.; Gallaway, J. W. Bismuth Enables the Formation of Disordered Birnessite in Rechargeable Alkaline Batteries. *J. Electrochem. Soc.* **2020**, *167*, 110514.
(54) Marschilok, A. C.; Bruck, A. M.; Abraham, A.; Stackhouse, C. A.; Takeuchi, K. J.; Takeuchi, E. S.; Croft, M.; Gallaway, J. W. Energy Dispersive X-Ray Diffraction (EDXRD) for Operando Materials Characterization within Batteries. *Phys. Chem. Chem. Phys.* **2020**, *22*, 20972−20989.